Materials Science & Engineering A 823 (2021) 141729

Contents lists available at ScienceDirect

Materials Science & Engineering A

journal homepage: www.elsevier.com/locate/msea

On mode II fracture toughness of sintered silver based on end-notch flexure (ENF) test considering various sintering parameters

Shuai Zhao [a], Yanwei Dai [a,b,*], Fei Qin [a,b,**], Yanning Li [a], Lingyun Liu [a], Zhi Zan [a], Tong An [a,b], Pei Chen [a,b], Yanpeng Gong [a,b], Yuexing Wang [c]

[a] Institute of Electronics Packaging Technology and Reliability, Faculty of Materials and Manufacturing, Beijing University of Technology, Beijing, 100124, China
[b] Beijing Key Laboratory of Advanced Manufacturing Technology, Faculty of Materials and Manufacturing, Beijing University of Technology, Beijing, 100124, China
[c] Institute of Electronic Engineering, China Academy of Engineering Physics, Mianyang, 621999, China

ARTICLE INFO

Keywords:
Sintered Ag
Mode II fracture Toughness
ENF test
Sintering parameter
Microstructure

ABSTRACT

Shearing fracture toughness of sintered silver (Ag) is an important parameter to reflect its shearing resistance. In this paper, mode II fracture toughness of sintered Ag is investigated based on end-notched flexure (ENF) test. Various sintering conditions are adopted to study the effect of sintering parameters on mode II fracture toughness of sintered Ag. The results show that the fracture toughness of sintered Ag increases rapidly with the increase of sintering temperature and holding time. Three shearing crack types are confirmed, i.e., interface delamination, tunneling cracking and cohesive cracking, and the cracking type varies from "interface delamination" or "tunneling cracking" to "cohesive cracking" with the increase of sintering temperature and holding time. An empirical equation is proposed to predict the mode II fracture toughness of sintered Ag. Through statistics investigation on microstructure evolution, it is found that the shearing fracture toughness heightens with enlargement of the Ag particle size, increase of the particle shape form factor, and decrease of the porosity. This study provides an alternative method to rigorously evaluate the shearing fracture toughness of die-attach materials in electronics packaging.

1. Introduction

To meet the growing demands on integration, miniaturization and energy conservation, silicon carbide (SiC) based wide band-gap semiconductors have been increasingly adopted in modern power electronic systems, which enable to be operated under faster switching speeds and higher temperature (over 250 °C) [1–4]. Traditional die-attach materials used in power electronic systems, such as lead-free solders and conductive adhesives, are not suitable for high temperature applications due to their low melting point and unsatisfactory thermal-mechanical reliability [5,6]. As a new type of interconnecting technique developed in recent years, sintered silver (Ag) has been regarded as an excellent candidate of die-attach materials adopted in SiC power electronic packaging due to its high melting point (960 °C), low electrical resistivity, low thermal resistivity, and excellent mechanical behaviors [7–9]. Since sintered Ag plays an important role to ensure heat dissipation and electrical interconnection in SiC power electronics, the investigations on failure mechanism and reliability evaluation for sintered Ag have drawn a lot of attentions in recent years [10–12].

During the operation processes of SiC power electronic modules, the power dissipation of the devices will lead to large fluctuation of junction temperature. Therefore, the interconnection layers are under shearing state due to remarkable discrepancy of coefficient of thermal expansion (CTE) of different layers, which will lead to the risk of cracking or delamination in the sintered Ag interconnects [13,14]. Hence, understanding the thermal-mechanical properties of sintered Ag comprehensively is necessary for reliability issues in the applications of SiC power module packaging. Although many efforts have been made to investigate various characteristics of sintered Ag, such as stress-strain curve [15–18], thermal conductivity [19–21], bonding strength [22–24] as well as their relationship with sintering parameter and microstructure [25–27], there are still many aspects which deserve to be further

* Corresponding author. Institute of Electronics Packaging Technology and Reliability, Faculty of Materials and Manufacturing, Beijing University of Technology, Beijing, 100124, China.
** Corresponding author. Institute of Electronics Packaging Technology and Reliability, Faculty of Materials and Manufacturing, Beijing University of Technology, Beijing, 100124, China.
E-mail addresses: ywdai@bjut.edu.cn (Y. Dai), qfei@bjut.edu.cn (F. Qin).

https://doi.org/10.1016/j.msea.2021.141729
Received 18 March 2021; Received in revised form 7 July 2021; Accepted 8 July 2021
Available online 10 July 2021

studied, e.g., fracture toughness is a very critical parameter to characterize the ability of cracking resistance for a material. Since microdefects such as pores and flaws form easily during Ag sintering process [28], it is particularly essential to understand the effect of sintering parameters on shearing fracture behaviors of sintered Ag.

Classical method to evaluate the fracture characteristics of sintered Ag is based on the die-shear or lap-shear test, which takes the maximum stress at the joint failure as the shearing strength [29–32]. Although those classical methods are adopted widely in industrial fields, they are not rigorous methods for fracture toughness measurement from the viewpoint of fracture mechanics. Recently, Chen et al. [33] investigated the fracture toughness of sintered Ag based on the middle-cracked specimen tensile and micro-cantilever bending tests. The results showed that the fracture toughness of the sintered Ag exhibited a distinct size effect, which was considered to be related to the variation of the ratio of grain boundary to grain volume. They also deduced that the fracture toughness of sintered Ag decreased with the increase of the pore size according to a two-dimensional finite element model simulation. Wang et al. [34] investigated the interfacial fracture behavior of sintered Ag on both copper (Cu) and gold (Au) metallized substrate through a modified compact tension test, the results revealed that the interfacial fracture toughness were affected by the microstructure and porosity evolution of sintered Ag. All these investigations on the fracture toughness measurement of sintered Ag are mainly focused on the mode I (opening-mode) fracture. However, as mentioned before, the stress generated in the sintered Ag interconnects are usually induced by the CTE mismatch of different layers, which usually causes large shearing stress of the interconnect structures. Hence, the assessment of mode II (shearing mode) fracture toughness of sintered Ag interconnects is also important and meaningful, however, investigations on this aspect reported in those available literatures are very limited.

The end-notched flexure (ENF) test was firstly proposed by Russell et al. [35] to perform the mode II fracture toughness by applying a three-point bending load to a double cantilever beam specimen. Due to its advantage of data reduction methods, it has been widely adopted to determine the mode II interlaminar fracture toughness of laminated composites and adhesives in recent years [36]. Huang et al. [37] studied the effect of interlayer phenylene oxide particles on the interlaminar fracture toughness of carbon-fiber-reinforced epoxy composites using ENF tests. Han et al. [38] investigated the effect of post curing parameters on the mode II fracture toughness of structural adhesive based on ENF test. Sousa et al. [39] further developed the ENF method to study the mode II fatigue delamination behavior of carbon/epoxy laminates. From those investigations, ENF test shows its powerful side in the evaluation of shearing fracture behaviors for different materials. It is very valuable to be adopted to assess the shearing fracture behaviors of electronic materials more accurately and reasonably in electronic packaging field.

The aim of this paper is to study the shearing fracture behaviors of sintered Ag under different sintering parameters through ENF test in a more rigorous manner. Towards this aim, the organization of this paper is given as following. The experimental procedures such as preparation of Cu/sintered Ag/Cu sandwich specimens are given in Section 2, where the method and theoretical foundation of ENF test is also illustrated. The solutions of ENF test, fracture morphology and microstructure for sintered Ag are presented in Section 3. The discussion of the sintering parameter and microstructure on the shearing fracture toughness is given in Section 4. The conclusions are drawn in the last section.

2. Experimental procedures

2.1. Material characterization

The Ag paste used in this paper is fabricated by Henkel Company (LOCTITE ABLESTIK SSP 2020). Fig. 1(a) shows the Ag particles before sintering observed by a field emission scanning electron microscope (FE-SEM, FEI Quanta 650). It can be seen that the Ag particles were composed of submicron Ag particles mixed with micron Ag flakes. Fig. 1 (b) presents the thermogravimetric analysis (TGA) and differential thermal analysis (DTA) traces of the Ag paste, which is measured by an integrated thermal analyzer (Hitachi TG/DTA 6300) during the processes that heating from room temperature to 300 °C in air atmosphere under the ramp rate of 10 °C/min. It can be seen from the TG curve that the weight of the Ag paste drops rapidly from 90 °C to 170 °C, and then decreases from 170 °C to 300 °C slowly. The total weight loss is around 8.6%, which is attributed to the solvent vaporization and organics decomposition [40]. The DTA curve shows that there exists a sharp exothermal peak around 240 °C, which is considered to be the combustion reactions of the organic matters [41]. Thus, the minimum sintering temperature is set as 240 °C as the fully decomposition of organics occurs at this temperature.

2.2. Specimen preparation and sintering parameter design

To evaluate the shearing fracture toughness of sintered Ag, Cu/sintered Ag/Cu sandwich ENF specimens were fabricated according to the processes shown in Fig. 2(a). Firstly, the surfaces of the pure Cu substrates were ground by 2000# SiC abrasive paper and then polished by 1 μm diamond paste to remove the native oxidation layers. All these Cu substrates after polishing were ultrasonically cleaned in acetone and ethanol each for 15 min to remove the residual particles and organic contaminants. Secondly, the Ag paste was printed on the lower Cu substrate with a 100 μm thick stainless-steel stencil and an un-printed zone with around 30 mm length was reserved at one end of the substrate as the pre-crack after bonding. Thirdly, two spacers of about 200 μm thick was placed on both edges of the lower Cu substrate with the

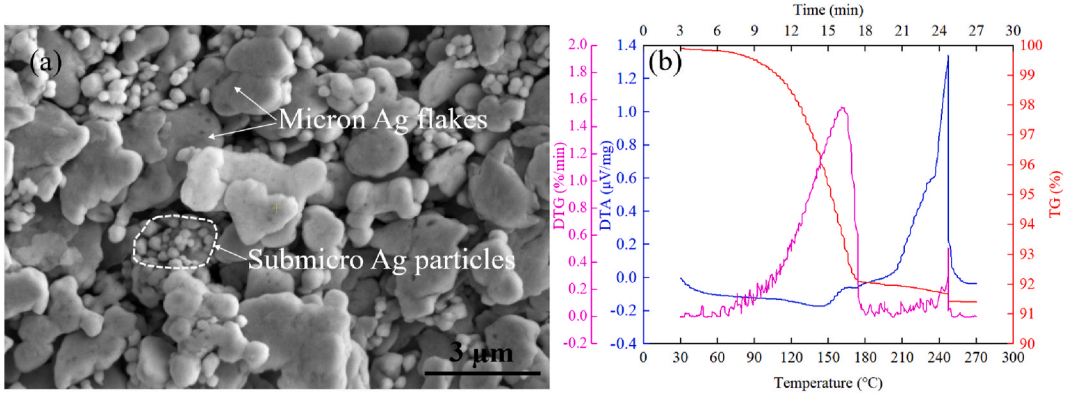

Fig. 1. Characterization of the Ag pastes adopted in the experiment. (a) SEM image of the Ag paste mixed with submicron Ag particles and micron Ag flakes; (b) TG and DTA traces of the Ag paste heated in air atmosphere under a ramp rate of 10 °C/min.

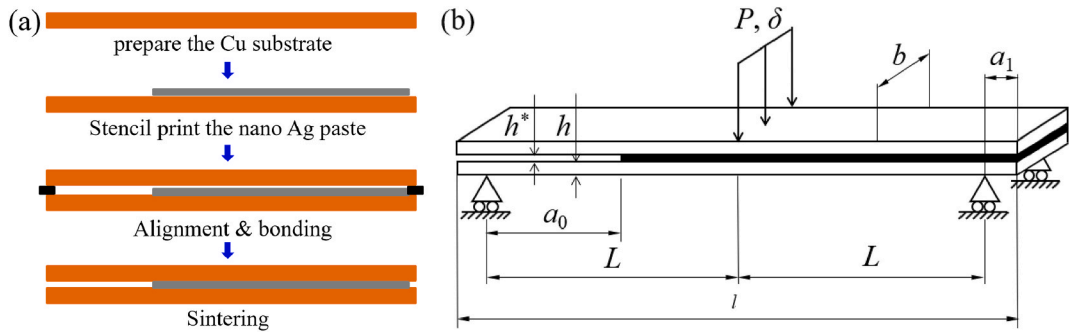

Fig. 2. Preparation of the ENF specimen. (a) Fabrication processes of the Cu/sintered Ag/Cu sandwich specimen for the ENF test; (b) Configuration of the ENF specimen.

lapped size of 3 mm. Then the polished side of the upper substrate was placed on the spacers and the position of the upper Cu substrate was adjusted manually to align the two substrates together. After alignment, the two spacers were drawn out in turn and the two substrates were bonded together. Finally, the sandwich specimens were placed in a lead-free reflow oven and sintered under different sintering parameters in air atmosphere.

A total of 12 sintering conditions are considered and the details are listed in Table 1. During the sintering process, a stainless jig is applied to fix the specimens and a pressure around 10 kPa is produced by gravity to guarantee fully contact of the upper substrates and Ag pastes. After the sintering processes, the specimens are naturally cooled down to room temperature. For each specimen, the overflowed Ag paste at the side wall and the notch caused by the spacer is removed through grinding with 800# SiC abrasive paper. The final configurations and dimensions of the specimens for ENF tests are shown in Fig. 2(b) and Table 2, respectively.

2.3. ENF test & data reduction methods

The ENF specimens were tested on the Instron 5948 micro tester with a three-point bending test loading fixture as shown in Fig. 3(a). The initial crack length, a_0, is set as $a_0 = 20.0$ mm and the loading speed for the ENF test is set as 0.2 mm/min. All the data of the load P and displacement δ during the loading processes are recorded for the subsequent data reduction to evaluate the concerned G_{IIC} of the sintered Ag interconnects with different sintering parameters. Fig. 3(b) shows a typical P-δ curve for brittle materials tested by ENF method, which includes three typical stages during the loading process [42]. At the initial stage, there exists a linearly uniform increase contributed by the elastic deformation, called “linear stage”. When the load increases to the critical load P_c, crack growth starts and the curve drops, which is called “crack growth stage”. When the crack propagates near the loading position, the resistance load for the specimen is then further increased, called “2nd increase stage”. In this paper, at least six ENF specimens were tested for each sintering condition to evaluate the shearing fracture toughness of sintered Ag.

Table 1
Sintering process parameters of the specimens for ENF tests.

Condition	Heating rate (s)	Sintering temperature (T)	Holding time (t)
No. 1	10 °C/min	240 °C	20 min
No. 2	10 °C/min	240 °C	40 min
No. 3	10 °C/min	240 °C	60 min
No. 4	10 °C/min	260 °C	20 min
No. 5	10 °C/min	260 °C	40 min
No. 6	10 °C/min	260 °C	60 min
No. 7	10 °C/min	280 °C	20 min
No. 8	10 °C/min	280 °C	40 min
No. 9	10 °C/min	280 °C	60 min
No. 10	10 °C/min	300 °C	20 min
No. 11	10 °C/min	300 °C	40 min
No. 12	10 °C/min	300 °C	60 min

Table 2
Dimensions of the specimens for ENF tests.

Parameter	Definition	Dimension (mm)
L	Total length	100.0
L	Half-span length	40.0
B	Width	8.0
a_0	Initial crack length	20.0
a_1	Distance from specimen edge to supporting point	10.0
H	Thickness of the substrate	1.2
h^*	Thickness of the sintered Ag paste	0.1

Data reduction methods for the ENF test are based on the theory of classical linear elastic fracture mechanics. According to Irwin-Kies equation, the mode II fracture toughness is presented as:

$$G_{IIC} = \frac{P^2}{2b}\frac{dC}{da}, \tag{1}$$

where $C = \delta/P$ is the compliance of the tested specimen, P is the applied loading, a is the depth of the crack and b is the width of the tested specimen. If $\delta/2L \ll 1$, the large deformation is negligible. Then the compliance C is written as following according to Euler beam theory [43],

$$C = \frac{2L^3 + 3a^3}{8Ebh^3}, \tag{2}$$

where E and h are elasticity modulus and the thickness of the copper substrate, respectively. Substituting Eq. (2) into Eq. (1), the shearing fracture toughness is expressed as

$$G_{IIC} = \frac{9P\delta a^2}{2b\left(2L^3 + 3a^3\right)}, \tag{3}$$

in which L is the length of the beam. This method is called Direct Beam Theory (DBT).

Several other methods such as Corrected Beam Theory (CBT) and Corrected Beam Theory with Effect crack length (CBTE) method were also been presented to consider the shear deformation of the beam and the effect of the fracture process zone (FPZ) [44]. However, all these methods require continuous monitoring of the crack growth length which is not easy to measure during the loading processes. For CBTE, additional bending test to determine the flexure modulus E_f is also inevitable. In recent years, a Compliance-Based Beam Method (CBBM) was proposed to eliminate the real-time monitoring of crack growth length and additional bending test [45]. According to Timoshenko beam theory, the compliance of the ENF specimen is expressed as [46]:

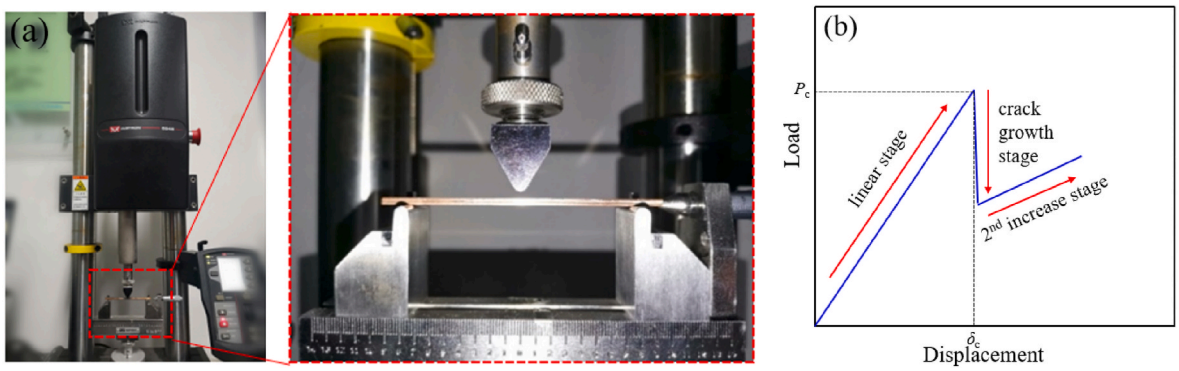

Fig. 3. The ENF test based on three-point bending method. (a) The ENF test and a close-up view of a specimen being tested by Instron 5948; (b) typical *P-δ* curve for brittle adhesive tested by ENF method.

$$C = \frac{2L^3 + 3a_e^3}{8E_f bh^3} + \frac{3L}{10Gbh}, \tag{4}$$

where E_f and G denote the flexural modulus and shear modulus of the substrate, respectively. a_e is the equivalent crack length of the ENF specimen. If E_f is known, a_e is easily given as:

$$a_e = \sqrt[3]{\frac{8E_f bh^3 C_c}{3} - \frac{2L^3}{3}}, \tag{5}$$

in which C_c is the corrected compliance which is defined with the following form:

$$C_c = C - \frac{3L}{10Gbh}. \tag{6}$$

In CBBM, an apparent longitudinal modulus E_a is obtained using the initial compliance C_0 and initial crack length a_0. According to Eq. (4), E_a can be expressed as:

$$E_a = \frac{3a_0 + 2L^3}{8Bh^3 C_{0c}}, \tag{7}$$

where C_{0c} is the corrected initial compliance which can be obtained from Eq. (6). Substituting the apparent modulus in Eq. (7) to the flexural modulus in Eq. (5), it will lead to

$$a_e = \sqrt[3]{\left[\frac{C_c}{C_{0c}} a_0^3 + \left(\frac{C_c}{C_{0c}} - 1\right)\right] \frac{2L^3}{3}}. \tag{8}$$

The combination of Eqs. (1), (4), (7) and (8) will lead to the following expression of the shearing fracture toughness G_{IIC}:

$$G_{IIC} = \frac{9P^2 C_{0c}}{2b\left(3a_0^3 + 2L^3\right)} \left[\frac{C_c}{C_{0c}} a_0^3 + \frac{2}{3}\left(\frac{C_c}{C_{0c}} - 1\right) L^3\right]^{2/3} \tag{9}$$

It can be seen that the G_{IIC} evaluation only requires the loading values and compliances of the specimens in CBBM. Moreover, the equivalent crack length can be evaluated by variations of corrected compliance according to Eq. (8), without additional crack length monitoring. Hence, CBBM is selected as the data reduction method for the G_{IIC} measurement in this paper.

2.4. Fracture morphology and microstructure observation

All the specimens after the ENF tests were placed upright and cold mounted by epoxy resign, respectively. After curing for 24 h, the mounted samples were ground by 200#, 400#, 800#, 1500# and 2000# SiC abrasive papers in turn and then polished using monocrystalline diamond suspensions with a grit size of 1 μm and 0.5 μm, respectively. A high-resolution optical microscope was used to observe the fracture morphology of the sintered Ag interconnects after ENF tests.

To quantitatively analyze the microstructure sintered Ag, the cross-section images were obtained by FE-SEM (FEI Quanta 650). For each sample, five SEM images were evenly taken along the un-cracked bond lines to measure the microstructure of sintered Ag. The "apparent" porosity, particle sizes and shape distributions of the sintered Ag were calculated according to a binary image analysis method which was accomplished using the ImageJ software. Firstly, the SEM images of the sintered Ag were converted to black and white binary images by threshold value analysis to extract the specific sintered Ag layers and the pore features with the Ag layers. The "apparent" porosity was calculated by measuring the proportion of the black areas in the whole areas. For the Ag particles size analysis, a watershed algorithm was done to segment the black areas, then the particle size distributions were obtained by measure the surface area of every segmentation considering a circular shape for all the particles. For the Ag particle shape, a shape form factor F is introduced to qualitatively characterize the Ag particle shapes according to the following equation:

$$F = \frac{4\pi A}{S^2} \tag{10}$$

where A is the measured Ag particle area and S is the measure Ag particle perimeter. The value of F varies between 0 and 1. If F approaches closer to 1, the Ag particle shape is more approaching a circle. If F approaches closer to 0, the particle shape is more approaching to elliptical and irregular. Details of above methods are given in Refs. [18,47,48].

3. Results

3.1. P-δ curves and fracture toughness of sintered Ag under different sintering parameters

The *P-δ* curves of the ENF specimens sintered under different conditions are shown in Fig. 4(a)–(d), respectively. It can be seen that all the *P-δ* curves of the tested specimens under each condition include the three typical stages as described in Section 2.2. Remarkable vertical drops are observed after the appearance of the first peak load, which indicates that the crack propagation in the sintered Ag is in accord with the fracture characteristics of brittle material [42]. The loading processes are terminated when the load increase for the second time is obviously observed. The reason is that G_{IIC} test is no longer valid when the crack has reached the vicinity of the loading head [38,43].

Table 3 and Table 4 list the critical load P_c and initial compliance C_0 for each specimen sintered under different conditions, respectively. All the P_c values vary within a small range for each sintering condition. Otherwise, the average initial compliances for the specimens sintered in all the conditions are 11.97 ± 0.93 μm/N. All these results indicate the relative low scatter of the *P-δ* curves and good repeatability of the ENF test to evaluate G_{IIC} of sintered Ag. Comparing the *P-δ* curves of the

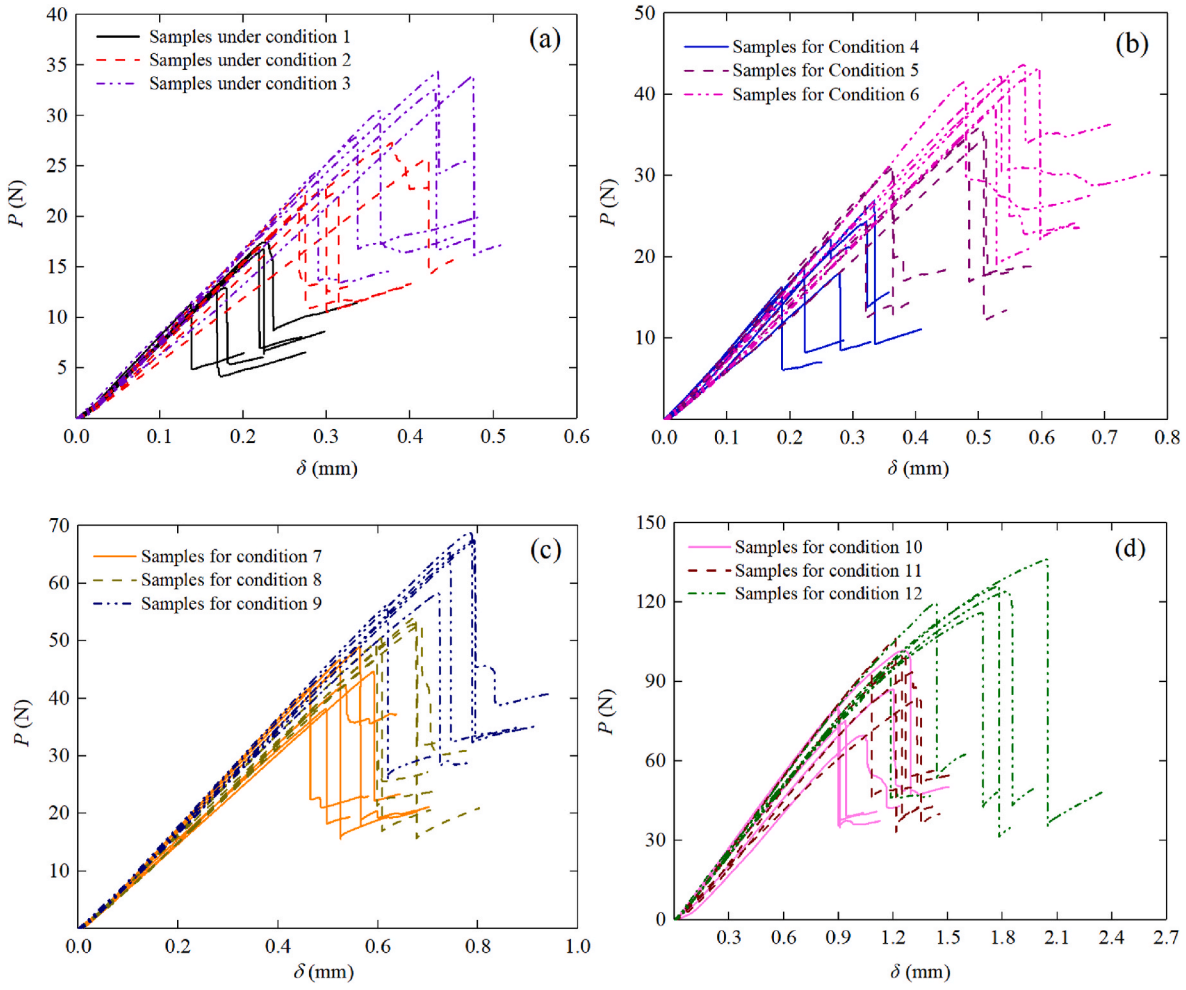

Fig. 4. *P-δ* curves of the ENF specimens sintering under different conditions. (a) 240 °C for 20/40/60 min; (b) 260 °C for 20/40/60 min; (c) 280 °C for 20/40/60 min; (d) 300 °C for 20/40/60 min.

Table 3
Critical loads *Pc* (N) of the ENF specimens sintered under different conditions.

condition	specimen 1	specimen 2	specimen 3	specimen 4	specimen 5	specimen 6
No. 1	16.85	16.79	12.57	11.30	12.97	17.46
No. 2	22.44	22.89	20.36	22.85	25.77	27.32
No. 3	30.47	27.86	24.50	32.66	33.98	34.31
No. 4	16.28	26.98	18.83	18.01	24.37	22.17
No. 5	27.90	30.97	31.36	36.07	34.53	34.57
No. 6	42.22	43.65	41.50	38.58	43.28	41.96
No. 7	48.91	41.80	46.70	42.25	44.65	38.20
No. 8	50.43	49.56	54.26	52.89	52.38	46.66
No. 9	67.46	68.78	65.34	67.13	56.19	58.23
No. 10	80.86	101.71	80.17	87.14	69.70	75.31
No. 11	95.77	99.88	106.20	82.43	98.92	93.50
No. 12	136.19	95.46	119.56	126.18	115.99	123.97

specimens sintered under different conditions, the critical load shows a strong relation with the sintering parameter. Comparing the *P-δ* curves of the specimens sintered under different conditions, the critical load shows a strong relation with the sintering parameter. It can be seen that the critical load increases with the prolonged holding time under a specific temperature. In general, the critical load also heightens significantly with the increase of sintering temperature. These results indicate that better shearing fracture properties can be obtained through improving sintering temperature and holding time.

To further study the mode II fracture toughness of the sintered Ag, the representative resistance curves (*R*-curves) are computed through CBBM method based on the tested *P-δ* curves, which connect G_{IIC} and a_e of the specimens after different sintering procedures. It is seen that the first stages of some *P-δ* curves in condition 11 and condition 12 exhibit an extent of nonlinearity which has been confirmed that this nonlinearity is mainly caused by the elastoplastic behavior of Cu substrates according to the analysis. Detail verifications of this point are given in the Appendix. It should be mentioned that the maximum relative errors for computation of fracture toughness with CBBM method caused by elastoplasticity of Cu substrate are lower than 10%. Hence, the CBBM method is still applicable in this study. Fig. 5 shows the calculated specific *R*-curves for different sintering conditions. Under each

Table 4
Initial compliances C_0 (μm/N) of the ENF specimens sintered under different conditions.

condition	specimen 1	specimen 2	specimen 3	specimen 4	specimen 5	specimen 6
No. 1	12.37×10^{-3}	12.68×10^{-3}	12.35×10^{-3}	11.64×10^{-3}	13.17×10^{-3}	12.47×10^{-3}
No. 2	11.06×10^{-3}	11.82×10^{-3}	12.58×10^{-3}	11.31×10^{-3}	13.91×10^{-3}	12.89×10^{-3}
No. 3	11.46×10^{-3}	11.41×10^{-3}	11.45×10^{-3}	12.81×10^{-3}	13.27×10^{-3}	12.54×10^{-3}
No. 4	11.06×10^{-3}	11.82×10^{-3}	11.30×10^{-3}	14.21×10^{-3}	12.00×10^{-3}	10.73×10^{-3}
No. 5	11.04×10^{-3}	11.16×10^{-3}	11.16×10^{-3}	12.42×10^{-3}	13.33×10^{-3}	12.28×10^{-3}
No. 6	12.09×10^{-3}	12.47×10^{-3}	10.88×10^{-3}	11.30×10^{-3}	11.16×10^{-3}	10.77×10^{-3}
No. 7	11.11×10^{-3}	10.69×10^{-3}	10.89×10^{-3}	12.17×10^{-3}	12.90×10^{-3}	12.78×10^{-3}
No. 8	11.68×10^{-3}	11.68×10^{-3}	11.99×10^{-3}	12.32×10^{-3}	12.41×10^{-3}	12.32×10^{-3}
No. 9	11.39×10^{-3}	11.01×10^{-3}	11.09×10^{-3}	11.38×10^{-3}	10.71×10^{-3}	12.06×10^{-3}
No. 10	10.82×10^{-3}	11.59×10^{-3}	10.81×10^{-3}	12.40×10^{-3}	13.34×10^{-3}	12.09×10^{-3}
No. 11	10.86×10^{-3}	11.56×10^{-3}	10.96×10^{-3}	12.36×10^{-3}	11.25×10^{-3}	11.87×10^{-3}
No. 12	14.28×10^{-3}	12.03×10^{-3}	11.45×10^{-3}	13.40×10^{-3}	13.80×10^{-3}	14.24×10^{-3}

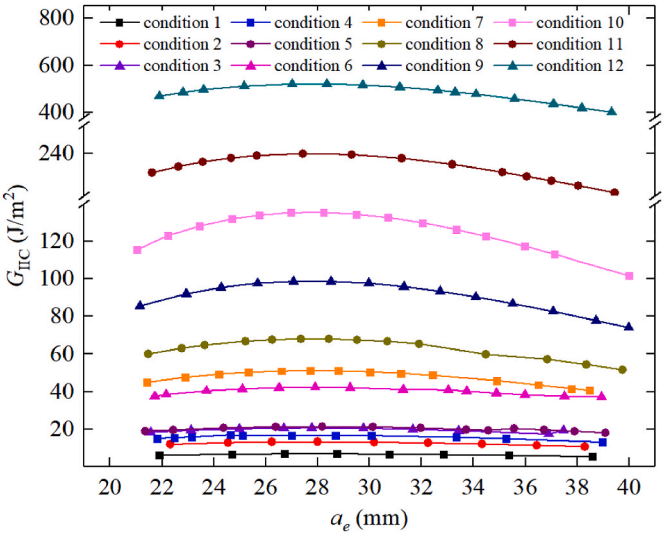

Fig. 5. *R*-curves of the tested ENF specimens sintered under different conditions.

condition, the critical shearing fracture toughness increases slightly first and then decreases when the equivalent crack length propagates approximately from 21.0 mm to 39.0 mm. Nevertheless, the variation rate is very slow, which indicates a relatively steady value. It should be noted that all the *R*-curves are trimmed before the equivalent crack lengths approaching to 40.0 mm, as the compressive effects induced by the loading head can not be negligible if the crack lengths are greater than 40.0 mm. The measured shearing fracture toughness for each specimen is determined by averaging all data in its *R*-curve. The average value and standard deviation of the calculated G_{II} for each specimen for each sintering condition are listed in Table 5 and the results will be discussed carefully in Section 3.4.

3.2. Fracture morphology of the sintered silver specimens

Fig. 6 shows the fracture morphologies for the sintered specimens after ENF tests obtained by a high-resolution optical microscope. All the cracking origins and paths of specimens are observed, and three shearing crack types are found in the ENF test even under shearing fracture model, including "interface delamination", "tunneling crack" and "cohesive crack", which are shown in Fig. 6 (b)–(d), respectively. The fraction of fracture types for the specimens sintered under various sintering conditions are summarized in Fig. 7. It can be seen that "interface delamination" and "tunneling crack" are the main fracture types for all the specimens sintered under conditions 1–9, in which the sintering temperature of the Ag pastes are not more than 280 °C. Whereas, as listed in conditions 10–12, "cohesive crack" dominates when the sintering temperature increases to 300 °C.

The fracture type transition indicates that the vulnerable point transits from the interface of sintered Ag/Cu to somewhere in the interior zone of the sintered Ag with the increasing of sintering temperature. The possible reason may be that the competition mechanism induced by the lattice mismatch of Ag/Cu and the stress concentration near the flaws or voids in the sintered Ag layer. Due to the difference of lattice constant between the Ag and Cu grains, the Ag particles are more easily bonded with each other than that with Cu substrate during the sintering processes [49]. Hence, the cracks propagate along the sintered Ag/Cu interface in most of those conditions. When sintering temperature increases to 300 °C, the interface is strong enough, during which the crack prone to propagate near the flaws or voids in the sintered Ag layer. Fig. 8 shows an SEM image of a typical crack tip of the sintered Ag/Cu interconnects. No obvious plastic deformation is observed at the crack tip zone. Such phenomenon suggests that the sintered Ag/Cu interconnects is characterized with brittle fracture property, which is consistent with the results of the *P*-*δ* curves in Section 3.1.

Table 5
G_{IIC} (J/m^2) of the ENF specimens sintered under different conditions using CBBM method.

condition	specimen 1	specimen 2	specimen 3	specimen 4	specimen 5	specimen 6	average	St. Dev.
No. 1	6.45	6.66	3.82	2.63	4.09	7.34	5.17	1.73
No. 2	12.48	12.04	9.58	10.58	18.64	20.35	13.95	4.07
No. 3	19.56	16.72	12.25	24.55	29.85	24.83	21.29	5.80
No. 4	5.26	15.81	7.20	8.39	13.11	9.81	9.93	3.57
No. 5	15.11	20.02	19.34	30.93	29.97	28.88	24.04	6.11
No. 6	40.69	46.15	37.92	34.64	43.84	38.97	40.37	3.79
No. 7	47.71	32.77	41.38	41.03	45.13	31.92	39.99	5.86
No. 8	50.61	48.72	62.75	65.79	61.49	48.75	56.35	7.13
No. 9	88.80	92.31	92.27	82.36	59.07	70.73	80.92	12.27
No. 10	125.37	236.73	121.46	188.98	152.19	120.36	157.52	42.83
No. 11	174.68	294.29	221.98	213.18	217.41	224.71	224.37	35.44
No. 12	460.78	194.46	304.17	376.46	321.16	351.47	334.75	80.32

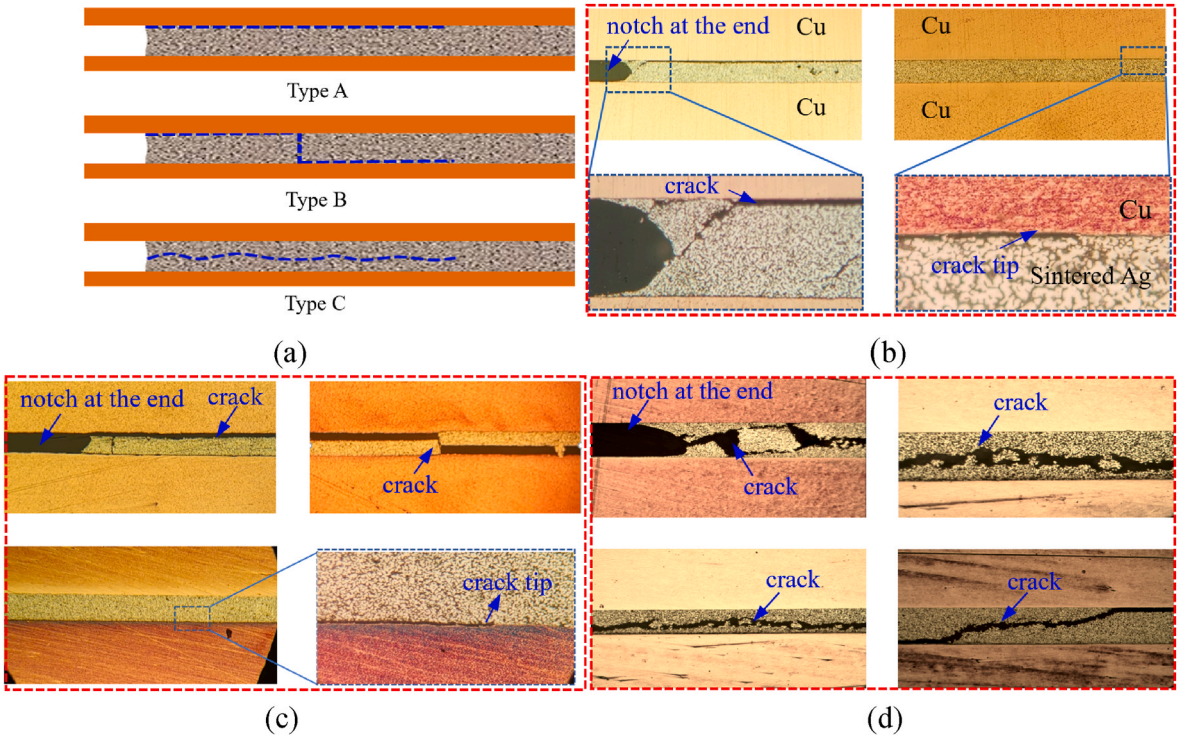

Fig. 6. Fracture morphology of the Cu/sintered Ag/Cu sandwich specimens after ENF test. (a) Schematic illustration of three main cracking modes: A: interface delamination; B: tunneling crack; C: cohesive crack; (b) Type A fracture morphology; (c) Type B fracture morphology; (d) Type C fracture morphology.

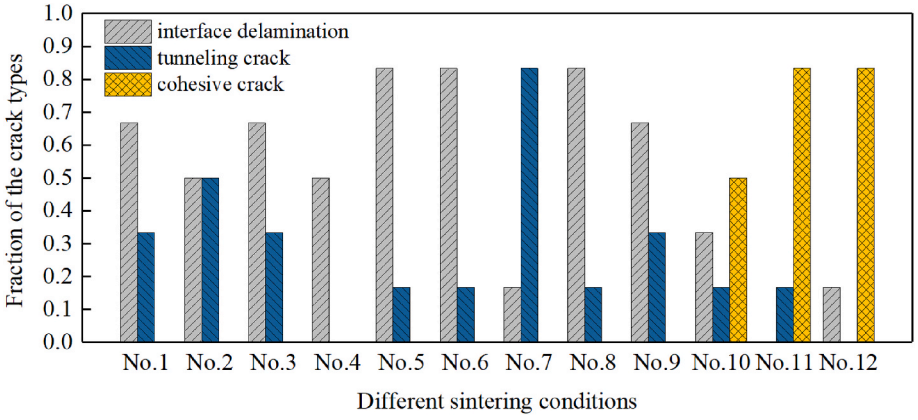

Fig. 7. Fraction of the fracture types of the specimens sintered under different conditions.

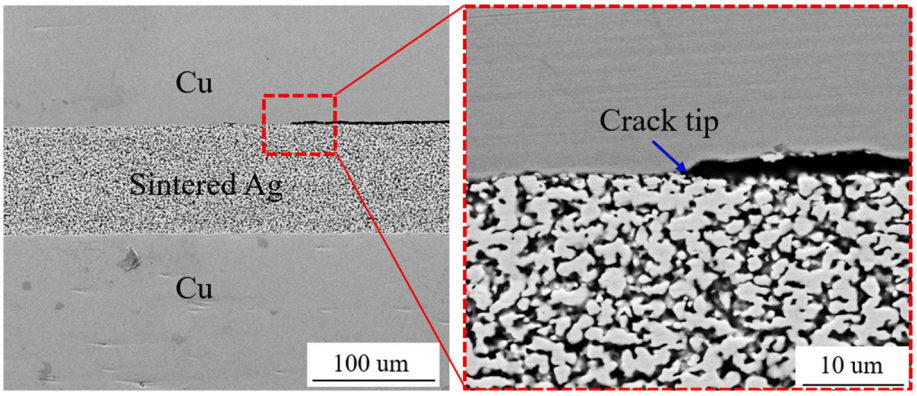

Fig. 8. A typical interface crack tip of a specimen after ENF test.

3.3. Microstructure of sintered Ag with different sintering parameters

The typical SEM images of the Ag pastes after sintering under different conditions are shown in Fig. 9, in which uniform porous structures and cross-linked Ag ligament networks are observed. In the SEM images, the black and white areas are the pores and sintered Ag, respectively. It can be seen that the organics have fully decomposed when the Ag pastes sintered in 240 °C for 20 min, and the Ag particles become coarsening and form very small necks, while most of them keep the initial shapes. With the increase of sintering temperature and holding time, the microstructures of the sintered Ag pastes tend to be denser, and sizes of the Ag particles keep growing. To quantitatively analysis the microstructure evolution of the Ag pastes sintered under different conditions, the Ag particle sizes, particle shape distributions and porosities are calculated through a binary image analysis method using ImageJ software, as described previously in Section 2.4.

The Ag particle sizes and distributions with different sintering parameters are shown in Fig. 10, in which the Ag particles are approximately treated as circles. It can be seen that all the distributions of the Ag particle diameters approximately obey Gaussian law, while the average particle diameters are positively related to the sintering temperature and holding time. Fig. 11 shows the detail variations of particle diameters with sintering temperature and holding time. It can be seen that the Ag particle diameters were only around 0.58 ± 0.33 μm when the Ag pastes sintered at 240 °C for 20 min, while it increased to 2.09 ± 0.74 μm when sintered at 300 °C for 60 min. It has been confirmed by many researchers that the mechanisms of particle size growth during sintering are contributed by lattice diffusion and grain boundary diffusion, and the particle size growth follows the principle of diffusion-controlled Ostwald ripening [50,51], which can be described as:

$$\frac{dD}{dt} = \frac{K_0}{D^2}\exp\left(-\frac{E_a}{RT}\right), \tag{11}$$

where D is the average particle diameter, t is the time, E_a is the activation energy, R is the gas constant, T is the absolute temperature and K_0 is a pre-exponential factor related to grain growth. Neglecting the effect of heating rate on the microstructure evolution of sintered Ag pastes, the relationship between average particle diameters and sintering temperature and holding time in this study can be expressed by the following equation:

$$D^3 = K_0 \exp\left(-\frac{E_a}{RT}\right)t + D_0^3, \tag{12}$$

in which D_0 is the initial particle size. Then transforming Eq. (12) into the logarithmic form:

$$\ln\left(D^3 - D_0^3\right) = \ln K_0 - \frac{E_a}{R}\frac{1}{T} + \ln t, \tag{13}$$

which indicates that $\ln(D^3\text{-}D_0^3)$ is a linear function of $1/T$ and t. A multiple linear regression analysis was applied to fit the data points. The parameters and the fitting surface are shown in Table 6 and Fig. 11, respectively. Good agreement between experimental data and fitting surface can be found. It can be seen that the average Ag particle size increases slowly with holding time at a relatively lower sintering temperature, while the average particle size increases faster at a relatively higher sintering temperature. The reason is that higher sintering temperature increases the migration energy of Ag atoms. Hence, the diffusion rate of lattice diffusion and grain boundary diffusion accelerates rapidly.

Fig. 12 shows the particle shape distributions of the Ag paste sintered under different conditions. It can be seen that the distributions of the Ag particle shapes also approximately obey Gaussian law, and the value of F also positively related to the sintering temperature and holding time. For the Ag pastes sintered at 240 °C for 20 min, the average value of F is 0.627, and the distributions of F are scattered with a higher standard deviation of 0.182. However, for the Ag paste sintered at 300 °C for 60 min, the average F increases to 0.720 and the distributions of F are more concentrated with a lower standard deviation of 0.095. These results indicate that the irregular Ag particle shapes gradually become rounder and more homogeneous with the increase of sintering temperature and prolonging of holding time. Such evolution may be related to the interdiffusion of the Ag particles and the action of surface energy.

Porosity of the Ag pastes sintered under different conditions are also calculated, and the average value and standard deviation in each condition are listed in Fig. 13. It can be seen that the average porosity of the Ag paste decreases with the increase of sintering temperature and

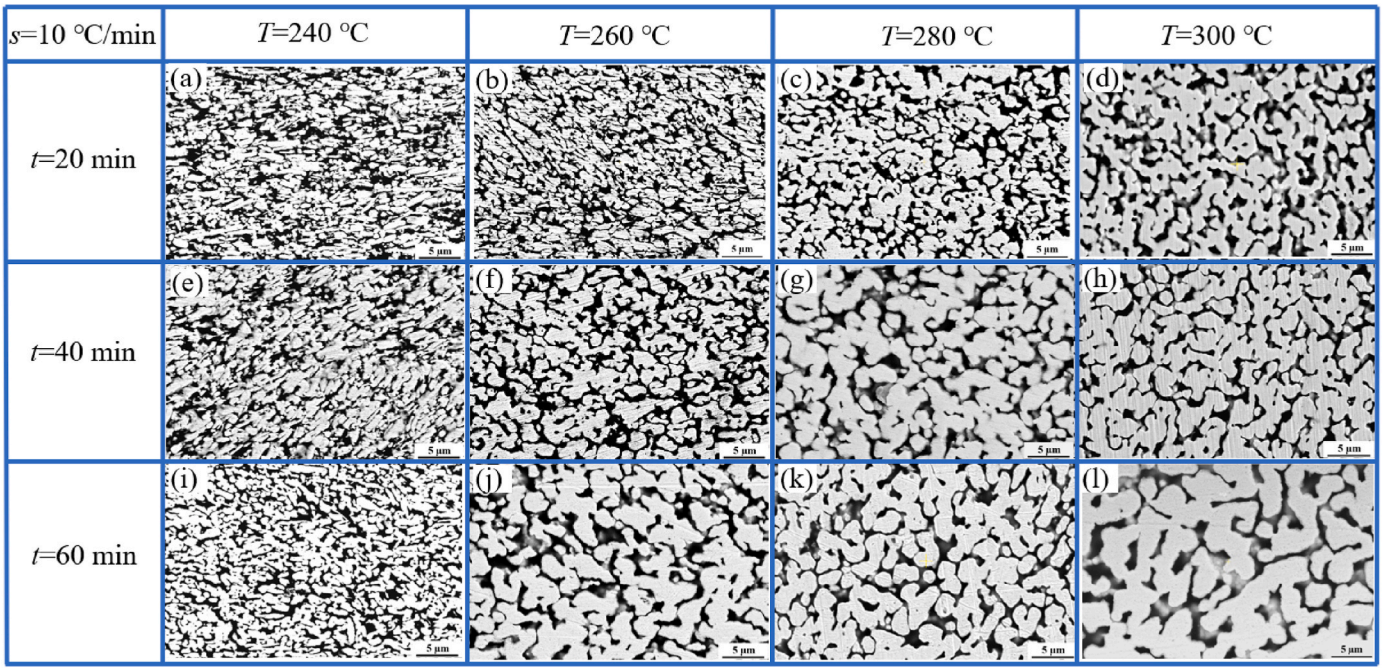

Fig. 9. The SEM images of sintered Ag for the ENF specimens considering different sintering parameters.

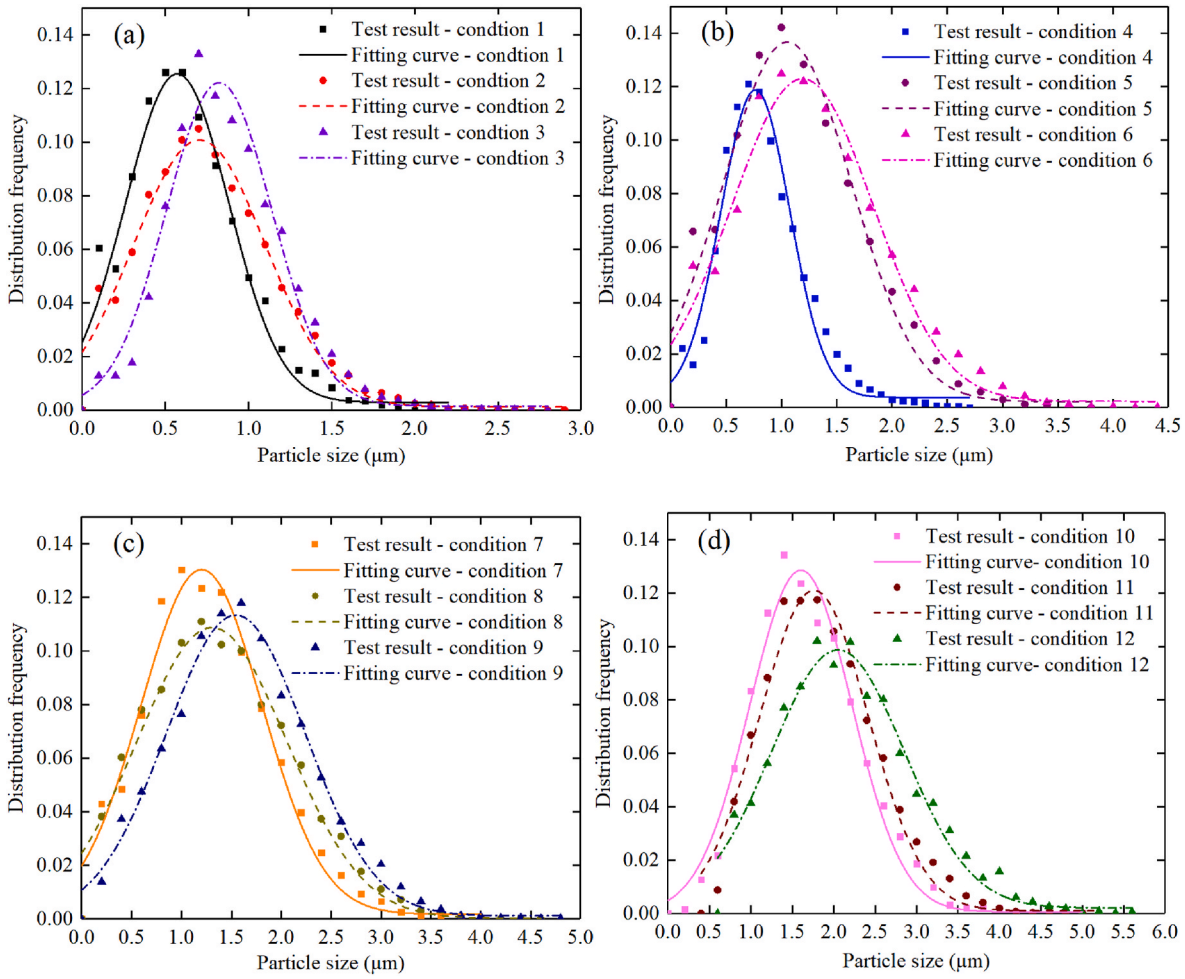

Fig. 10. Particle size distributions of the Ag pastes sintered under different conditions. (a) 240 °C for 20/40/60 min; (b) 260 °C for 20/40/60 min; (c) 280 °C for 20/40/60 min; (d) 300 °C for 20/40/60 min.

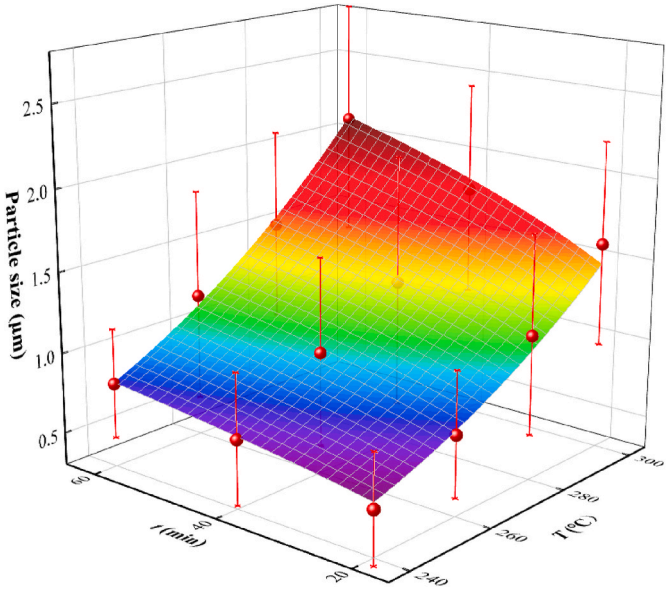

Fig. 11. Relationship between average Ag particle sizes and sintering temperature and holding time.

Table 6
Material parameters of the multiple linear regression analysis of Ag particle sizes using Eq. (13).

K_0 (μm^3/s)	E_a (kJ/mol)	R (J/(mol•k))
7.27×10^7	110.6	8.314

holding time. When the Ag paste sinters at 240 °C for 20 min, the porosity of sintered Ag is 34.38% ± 2.25%. However, it decreases to 24.08% ± 0.84% when the Ag paste sinters at 300 °C for 60 min. The densification mechanism of the sintered Ag can also be explained by the diffusion theory during sintering and the typical densification rate equation is expressed as [52,53]:

$$\frac{1}{\rho}\frac{d\rho}{dt} = -C_1 n t^{n-1} \exp\left[-\frac{E_a}{RT}\right], \tag{14}$$

where ρ is the normalized density, E_a is the apparent activation energy, C_1 is a pre-exponential factor and n is a constant related to the diffusion mechanism with a value in between of 1/3 to 1 [52,54]. In this paper, we take $n = 1/3$ due to a higher accuracy is obtained with this value. Defining the porosity of the Ag paste as $p = 1\text{-}\rho$, then the relationship between porosity and sintering temperature and holding time can be expressed as:

$$\ln\left[\frac{p}{p_0}\right] = -C_2 t^{1/3} \exp\left[-\frac{E_a}{RT}\right], \tag{15}$$

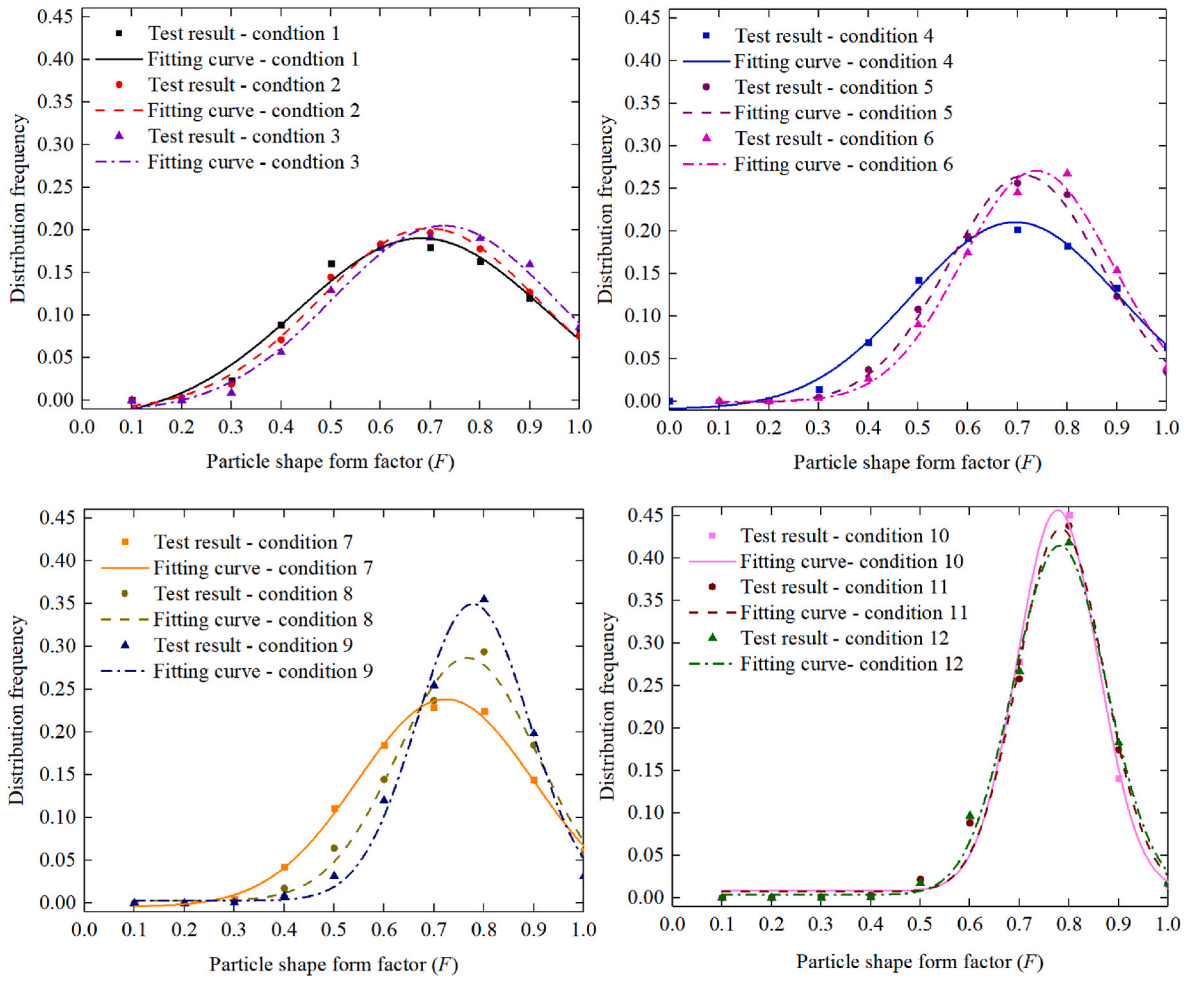

Fig. 12. Particle shape distributions of the Ag pastes sintered under different conditions. (a) 240 °C for 20/40/60 min; (b) 260 °C for 20/40/60 min; (c) 280 °C for 20/40/60 min; (d) 300 °C for 20/40/60 min.

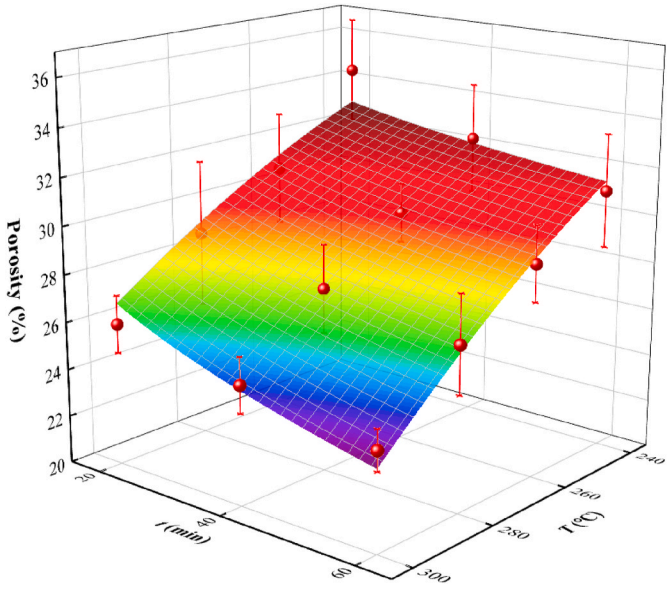

Fig. 13. Relationship between average porosities of the Ag pastes and sintering temperature and holding time.

where C_2 is a constant and p_0 is the initial porosity. Similarly, a multiple linear regression analysis is also applied by transforming Eq. (15) into logarithmic form. The parameters and the fitting surface are shown in Table 7 and Fig. 13, respectively. Good agreements between experimental statistics and fitting curve are also found. It can be seen that the average porosity decreases slowly with the increase of holding time, whereas decreasing faster with the increase of sintering temperature. Through the microstructure quantification analysis, it is confirmed that both the Ag particle growth and densification consistent with the kinetic theory of sintering [53], in which sintering temperature and holding time are very important variables to affect microstructure evolution. Furthermore, it can be concluded that the effect of sintering time on the porosity is typically less than that of sintering temperature.

4. Discussion

4.1. Effect of sintering parameters on mode II fracture toughness of sintered Ag

Fig. 14 summarizes the average G_{IIC} calculated by CBBM according

Table 7
Material parameters of the multiple linear regression analysis of Ag particle sizes using Eq. (15).

C_2	E_a (kJ/mol)	R (J/(mo·k))
230.04	94.67	8.314

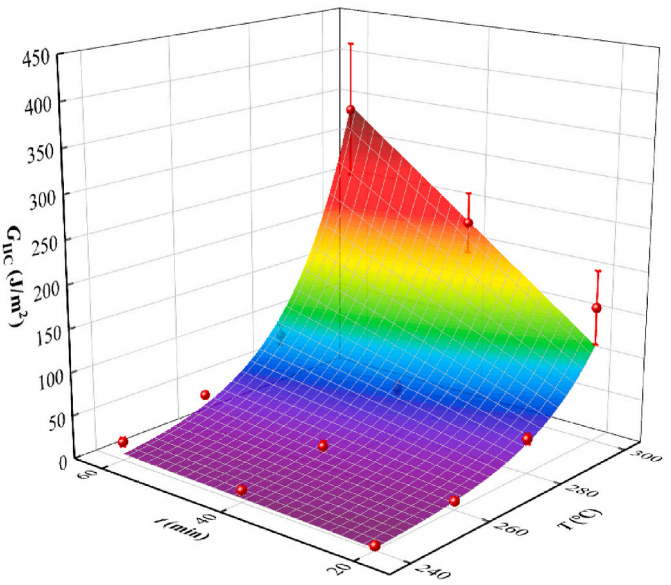

Fig. 14. Relationship between the average G_{IIC} and sintering temperature and holding time.

to all the *P*-*δ* curves tested by all the specimens sintered under different conditions. It is concluded that the shearing fracture toughness of the Cu/sintered Ag/Cu interconnects shows a strengthening tendency with the increase of sintering temperature as well as holding time. The shearing fracture energy is 5.20 ± 1.82 J/m^2 when the Ag pastes are sintered at 240 °C for 20 min. However, the mode II fracture toughness reaches as high as 345.47 ± 92.41 J/m^2 when sintered at 300 °C for 60 min, which is about 66 times of the former condition. Furthermore, the effect of sintering temperature on G_{IIC} of Cu/sintered Ag interconnects are much greater than that of holding time. To explain this, an empirical model is presented to characterize the relationship between G_{IIC} and sintering temperature and holding time and expressed as:

$$G_{IIC} = G_0 \exp\left(-\frac{E_a}{RT}\right)t, \tag{16}$$

in which G_0 is a pre-exponential factor, E_a is the activation energy, R is the gas constant, T is the absolute temperature and t is the holding time. The equation can be deduced by the following. As is known, the bonding mechanism of the Cu/sintering Ag depends on the formation of metallic bond caused by the atomic diffusion during the sintering process [55]. Assuming that the surface energy γ is proportional to the number of Ag–Cu and Ag–Ag bonds, N_m, then the following relation is assumed:

$$\frac{d\gamma}{dt} \propto \frac{dN_m}{dt} \tag{17}$$

where $d\gamma/dt$ and dN_m/dt are denoted as the variation rate of surface energy and the number of metallic bonds during sintering process, respectively. If one assumes dN_m/dt is proportional to the atomic diffusion rate, k, according to Arrhenius equation [56]:

$$\frac{d\gamma}{dt} \propto \frac{dN_m}{dt} \propto k = k_0 \exp\left(-\frac{E_a}{RT}\right), \tag{18}$$

in which k_0 is a pre-exponential factor. Then the dependence of surface energy on sintering temperature and holding time can be expressed by the equation below:

$$\gamma = \gamma_0 \exp\left(-\frac{E_a}{RT}\right)t, \tag{19}$$

in which γ_0 is the pre-exponential factor. According to Griffith's theory [57], the critical energy release rate G_C should be identical to 2γ, Thus, Eq. (16) can be easily obtained. Through multiple linear regression curve fitting, the parameters of Eq. (16) are obtained directly which have been shown in Table 8. The variations of G_{IIC} with sintering temperature and holding time are shown in Fig. 14. The result shows a quite strong relation between G_{IIC} and sintering temperature and holding time. Furthermore, the effect of sintering temperature on G_{IIC} are obviously more remarkable than that of holding time. This phenomenon can be well predicted by Eq. (16) as the effect of sintering temperature on G_{IIC} follows an exponential relation while the effect of holding time on G_{IIC} follows a linear relation. The results indicate that the relationship of shearing fracture toughness on the sintering parameters are also attributed to the kinetic theory of sintering, as the surface energy are dependent with the atomic diffusion behavior during sintering process. It is interesting that the apparent activation energy fitted by Eq. (16) is close to those computational results based on the microstructure evolution in Section 3.3, which indicates that the mode II fracture toughness and microstructure of sintered Ag are highly interlinked.

Although the shearing fracture toughness of sintered silver can be improved at higher temperature, the silver pastes are not recommended to be sintered at a very high temperature in the current industrial background, even its melting point exceeds 960 °C. The reason is that other packaging materials and devices at front-end-of-line could not endure such high temperatures during packaging process if the sintered temperature exceeds 300 °C, which will lead to other reliability issues, such as copper oxidation, substrate warpage and some other physical failures. Hence, it needs a balance between increase of sintering temperature and manufacturing requirements.

4.2. *Effect of microstructure on the mode II fracture toughness of sintered Ag*

Fig. 15 plots the variations of average mode II fracture toughness G_{IIC} with the microstructure parameters D, F and p. From Fig. 15, a clear relationship between G_{IIC} and the average particle sizes, particle shapes and porosities of the sintered Ag pastes can be found. It is seen that the Ag microstructure presents a small particle size, irregular shape distribution, and high porosity after sintering at low temperature and short holding time, which leads to the low average G_{IIC}. With the increase of the sintering temperature and holding time, the size and density of Ag particle increases consistently, and the Ag particle shape become rounder and more homogeneous, which lead to the increase of G_{IIC}. It is concluded that the combinational effect of the Ag particle growth, Ag particle shape rounding and uniformization and porosity reduction lead to the significant reinforce of mode II fracture toughness of sintered Ag. Similar results have been also reported by Gu et al. [58] and Eatemadi et al. [59] in the study of sintered ceramics.

The main reasons for the effect of Ag particle size on mode II fracture toughness of the sintered Ag could depend on the following aspects. On one hand, the sintered Ag with smaller particles size exists a higher ratio of grain boundary and grain volume, which may increase the probability of crack propagation, as the crack usually propagates along the grain boundary [33]. On the other hand, larger Ag particle size with strong neck can arrest the crack propagation by the mechanism of crack deflection, which need more energy during micro-crack propagation [58]. As to the Ag particle shapes, rounder and more homogeneous particle shapes are benefit for the interdiffusion of Ag particles. Otherwise, irregular particle shapes lead to more inhomogeneous and angular for the pores, which will increase the stress concentration in the sintered Ag layer [60]. Thus, the shearing fracture toughness is reduced.

Table 8
Material parameters of the multiple linear regression analysis of G_{IIC} using Eq. (16).

G_0 (J/(m^2•s))	E_a (kJ/mol)	R (J/(mol·k))
1.84×10^{13}	136.7	8.314

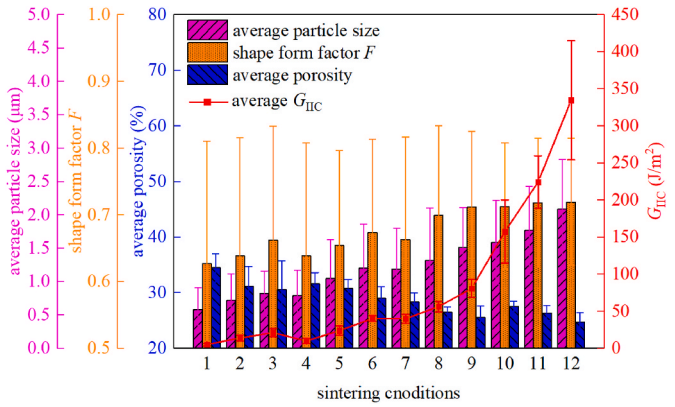

Fig. 15. Relationship between the average G_{IIC} and microstructure of the sintered Ag interconnects.

The effect of porosity on the mechanical properties of sintered Ag has been widely investigated, common results were obtained that lower densification has been found to lead to lower tensile strength and ductility [18,21]. The effect of porosity on the mode II fracture toughness are also analogous to the former studies. The increase of G_{IIC} with the porosity reduction can be attributed to the increase of actual cracking areas according to the investigation of cellular solids by Gibson et al. [61]. They considered that the ratio of G^*_C/G_C, where G^*_C and G_C are denoted as the fracture toughness of the porous and the dense material, is equal to the ratio of the substantial crack area to the total crack area. In other words, the reduction of porosity increases the actual load bearing surface, which will increase the measured fracture toughness value accordingly.

5. Conclusions

In this paper, mode II fracture toughness of sintered Ag is evaluated through ENF test. The effect of sintering parameters and microstructure on the mode II fracture toughness of sintered Ag are presented. Based on the study, the conclusions are drawn as below:

1. Through ENF test, it is found that the sintering parameters have a significant effect on mode II fracture toughness of sintered Ag, which increases rapidly with the increase of sintering temperature and holding time. It should be noted that the effect of sintering temperature plays a more important role than that of holding time.
2. Three different cracking types are found in the mode II fracture test, and the cracking type varies from “interface delamination” or “tunneling cracking” to “cohesive cracking” with the increase of sintering temperature and holding time. When sintered at 300 °C, the “cohesive cracking” is dominated.
3. The size and density of sintered Ag particle increase with the augment of sintering temperature and holding time, and the Ag particle shape becomes rounder and more homogeneous. An empirical model is established to characterize the relationship between G_{IIC} and sintering temperature and holding time. The presented model can be well explained by the diffusion mechanism of Ag atoms.
4. It is deduced that the shearing fracture toughness of the sintered Ag is significantly affected by Ag particle size, particle shape and porosity. The shearing fracture toughness increases with the growth of Ag particle size, increase of shape form factor, and decrease of Ag porosity. The growth of Ag particle size reduces the proportion of grain boundary and blocks the crack propagation by the mechanism of crack deflection. The rounding and homogeneous of Ag particle shape decreases the stress concentration in the sintered Ag layer. The porosity reduction increases the effective loading bear area. The crack propagation in sintered Ag needs more crack driving force for these cases, which leads to the increase of the shearing fracture toughness.

It is found that the shearing behavior of sintered Ag can be evaluated properly through ENF test, which indicates that ENF method can be adopted to evaluate the mode II fracture toughness for electronic packaging materials. It is very hopeful that this method can be extended to evaluate the mode II cracking behaviors of other electronic packaging materials in the future. More works on the shearing fracture toughness of sintered Ag bonded with different metallization substrates and its evolution during long-term high temperature environment based on ENF test are now in progress and will be reported later.

CRediT authorship contribution statement

Shuai Zhao: Methodology, Software, Data curation, Investigation, Writing – original draft. **Yanwei Dai:** Conceptualization, Writing – review & editing, Funding acquisition, Supervision. **Fei Qin:** Writing – review & editing, Project administration, Supervision. **Yanning Li:** Formal analysis, Investigation. **Lingyun Liu:** Visualization, Investigation. **Zhi Zan:** Validation, Investigation. **Tong An:** Writing – review & editing. **Pei Chen:** Writing – review & editing. **Yanpeng Gong:** Writing – review & editing. **Yuexing Wang:** Software.

Declaration of competing interest

The authors declare that they have no known competing financial interests or personal relationships that could have appeared to influence the work reported in this paper.

Acknowledgment

The authors acknowledge the support from the Beijing Municipal Natural Science Foundation (2204074), the National Natural Science Foundation of China (11902009), and the Scientific Research Common Program of Beijing Municipal Commission of Education (KM202010005034).

Appendix. The influences of elastoplastic behavior for Cu substrate on the CBBM method for calculating shearing fracture toughness

In order to determine the influence of elastoplastic behaviors for Cu substrates on the computational accuracy of CBBM method, a finite element analysis combined with the cohesive zone model CZM) using ANSYS 18.0 is introduced. Full details about this method can refer to the following two references [43,45]. The element type of the Cu and stainless steel (the three-point bending fixture) are chosen as Solid 185, and the element type of adhesive layer is chosen as Inter 205. Fig. A1 shows the 3D finite element model and boundary conditions of the ENF test. A mode II dominated bilinear traction-separation law for CZM model is introduced as shown in Fig. A2, in which t_t^{max} is the maximum tangential cohesive traction, δ_t^* is the tangential displacement jump at maximum tangential cohesive traction and δ_t^c is the tangential displacement jump at the completion of debonding. The area of the triangle is equal to the mode II fracture toughness G_{IIC}.

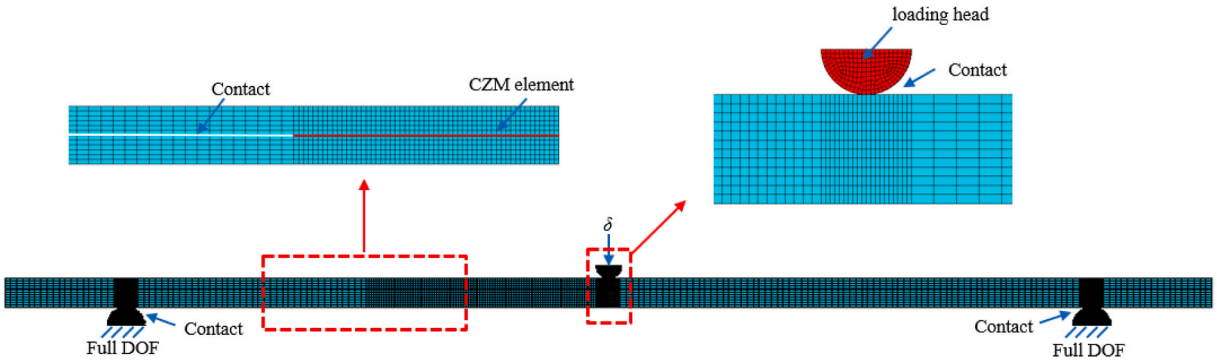

Fig. A1. 3D finite element model and boundary conditions of the ENF test.

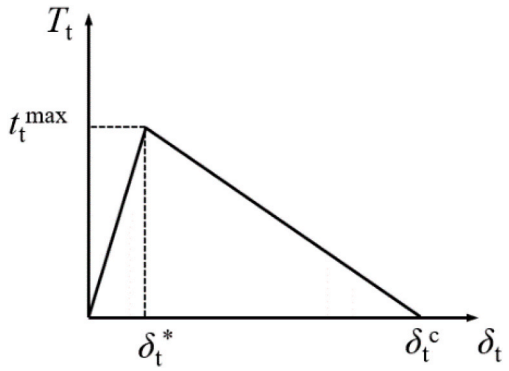

Fig. A2. Mode II dominated bilinear traction-separation law for CZM model.

One of the tested *P-δ* curves in condition 12 is taken to validate the simulation model. The material property of the stainless steel is regarded as isotropic elastic and the Cu substrate is considered to be a bilinear isotropic hardening elastic-plastic model. The details of the material properties are listed in Table A1. In the CZM model, the t_t^{max} is set as 50 MPa which is equal to the shearing strength of sintered Ag [29]. It has been proved that the ratio of δ_t^* to δ_t^c is less important and the value is set as 0.1 in this model [62]. Then δ_t^c is estimated by an inverse fitting technique until the numerical *P-δ* curve exhibits a good agreement to the experimental curve. The convergence of the simulation result is verified with different mesh densities, and the number of adopted element is 77059. An isotropic elastic model of Cu is also applied with the same CZM parameters to compare the effect of Cu material properties on the *P-δ* curves. Fig. A3 shows the comparison of the experimental and numerical *P-δ* curves, at which the δ_t^c in the CZM model is 1.68×10^{-2} mm. The numerical result based on the elastic-plastic model matches with the experiment results well. However, for the elastic model, the first stage of the *P-δ* curve keeps high linearity. These results indicate that the nonlinearity of the *P-δ* curve is mainly caused by the elastic-plastic property of the Cu substrate.

Table A1
Material properties adopted in the finite element model.

Materials	Elasticity modulus (GPa)	Poisson's ratio	Yield strength (MPa)	Tangent modulus (GPa)
Cu	115	0.236	219	6.5
Stainless steel	250	0.29	–	–

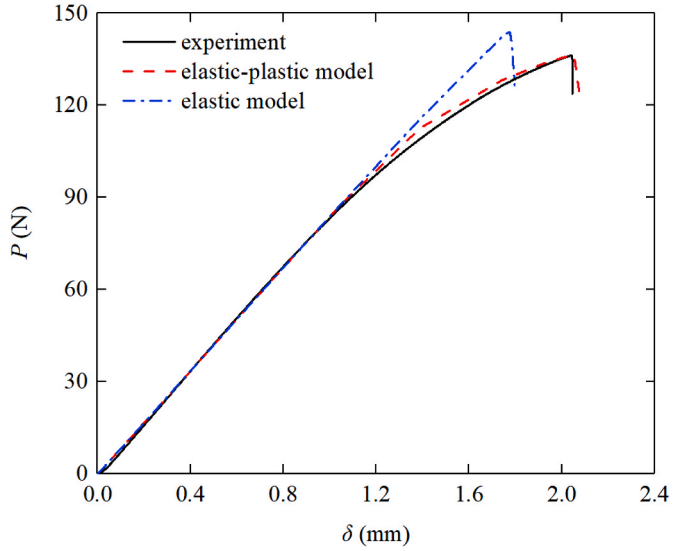

Fig. A3. Comparison of the tested *P*-δ curve and the numerical *P*-δ curves based on different Cu material properties.

To quantitatively characterize the effect of this nonlinearity (elastoplasticity of Cu substrate) on the computational accuracy of CBBM method, we define an indicator to reflect the effect of nonlinearity on the *P*-δ curve which is expressed as:

$$\text{nonlinearity} = \frac{\delta_a - \delta_e}{\delta_e}. \tag{20}$$

where δ_a is the displacement at the critical load in the numerical *P*-δ curve based on elastic-plastic model, and δ_e is the displacement at the same critical load by assuming that no plastic deformation occurs (As shown in Fig. A4, the red dashed line is the fitted line of the linear stage in the *P*-δ curve using least square method, and point ***O*** is the intersection of the fitted line and line $P=P_c$. δ_e is defined as the displacement corresponding to point ***O***). The results of mode II fracture toughness obtained by the numerical method and that obtained by CBBM method are listed in Table A2, in which G_{IIC}^{N} is obtained by the CZM parameters (the triangle area) and G_{IIC}^{CBBM} is calculated based on the CBBM method according to the numerical *P*-δ curves. The relative error is defined as:

$$\text{relative error} = \frac{G_{IIC}^{N} - G_{IIC}^{CBBM}}{G_{IIC}^{N}} \cdot 100\%. \tag{21}$$

It can be seen from Table A2 that when the nonlinearity is 0%, the relative error of the CBBM method is only 1.36%. When the nonlinearity is 0.261, the relative error of the CBBM method increases to 9.74%.

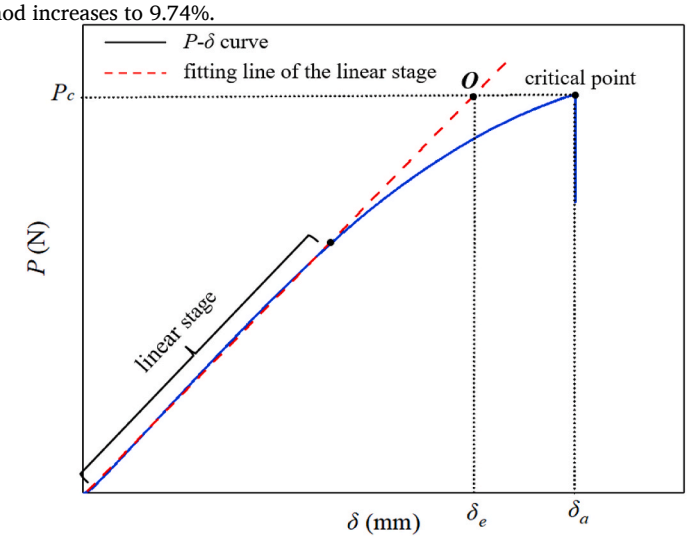

Fig. A4. The definition of δ_e and δ_a.

Table A2
Comparation of the G_{IIC} obtained by numerical method and CBBM.

simulation model	Nonlinearity	G_{IIC}^{N} (J/m^2)	G_{IIC}^{CBBM} (J/m^2)	relative error (%)
Elastic	0	420	425.7	1.36
elastic-plastic	0.261	420	460.9	9.74

We further change δ_t^c to investigate the effect of different nonlinearities on the relative error of the CBBM method. Fig. A5(a) shows the different numerical *P*-δ curves and Fig. A5(b) shows the variations of relative error with the change of material nonlinearity. It can be seen that the relative error approximately increases linearly with the nonlinearity. When the nonlinearity increases to 0.395, the relative error increases to 14.6%. Fig. A6(a) and Fig. A6(b) show all the tested *P*-δ curves of condition 11 and condition 12, respectively. All the nonlinearities are calculated and listed in Table A3. It can be seen that all the specimens more or less exhibit an extent of nonlinear, however, all the nonlinearities are at a relative low level (no more than 0.261). According to Fig. A5(b), it is concluded that the relative errors of CBBM for these conditions are all under 10%.

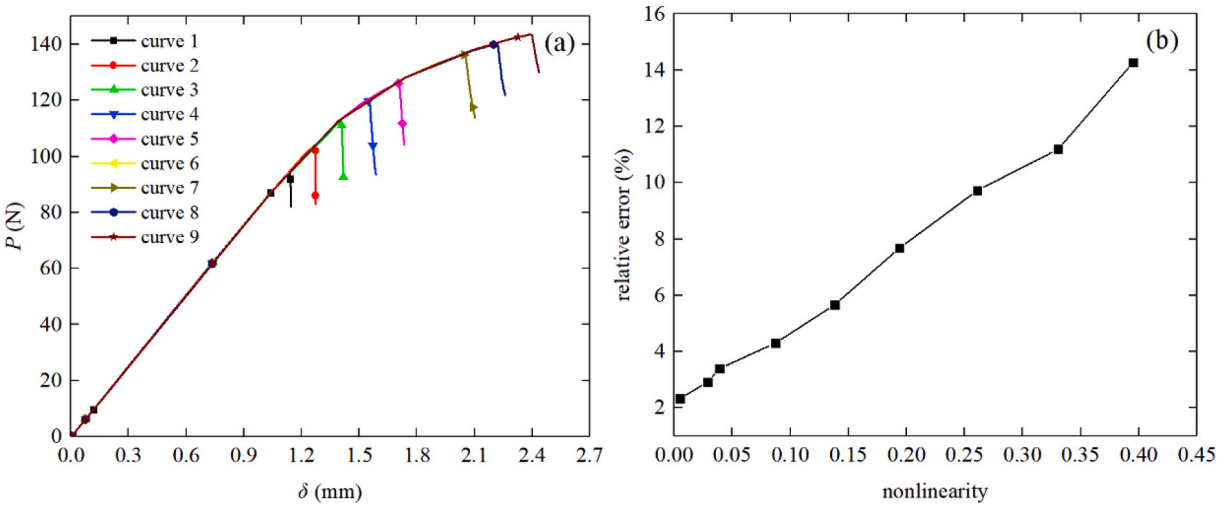

Fig. A5. Effect of nonlinearity of different *P*-δ curves on the accuracy of CBBM method. (a) Different *P*-δ curves obtained by different CZM parameters; (b) the relationship between nonlinearity and relative error.

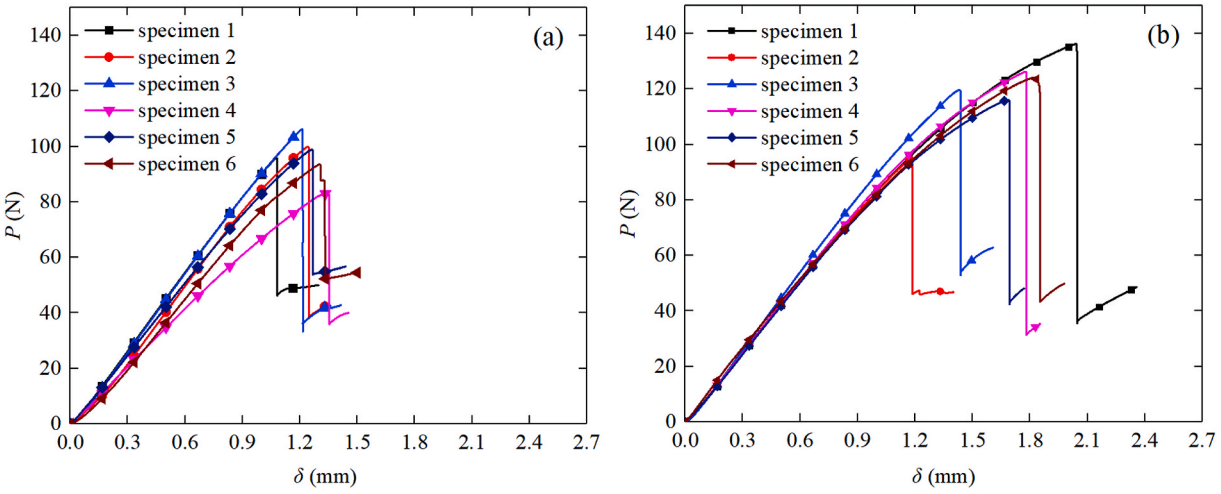

Fig. A6. The tested *P*-δ curves for the specimens sintering at conditions 11–12. (a) Condition 11; (b) condition 12.

Table A3
Nonlinearity for all the specimens tested in condition 11 and condition 12.

Condition 11	Nonlinearity	Condition 12	Nonlinearity
specimen 1	0.051	specimen 1	0.261
specimen 2	0.069	specimen 2	0.058
specimen 3	0.067	specimen 3	0.019
specimen 4	0.111	specimen 4	0.223
specimen 5	0.077	specimen 5	0.213
specimen 6	0.132	specimen 6	0.217

References

[1] J. Fabre, P. Ladoux, M. Piton, Characterization and implementation of dual-SiC MOSFET modules for future use in traction converters, IEEE Trans. Power Electron. 30 (8) (2015) 4079–4090.
[2] X. She, A.Q. Huang, Ó. Lucía, B. Ozpineci, Review of silicon carbide power devices and their applications, IEEE Trans. Ind. Electron. 64 (10) (2017) 8193–8205.
[3] Q. Xun, B. Xun, Z. Li, P. Wang, Z. Cai, Application of SiC power electronic devices in secondary power source for aircraft, Renew. Sustain. Energy Rev. 70 (2017) 1336–1342.
[4] F. Roccaforte, P. Fiorenza, G. Greco, R.L. Nigro, F. Giannazzo, F. Lucolano, M. Saggio, Emerging trends in wide band gap semiconductors (SiC and GaN) technology for power devices, Microelectron. Eng. 187–188 (2018) 66–77.
[5] T. Laurila, V. Vuorinen, J.K. Kivilahti, Interfacial reactions between lead-free solders and common base materials, Mater. Sci. Eng. R Rep. 49 (2005) 1–60.
[6] H. Zhang, J. Minter, N.C. Lee, A brief review on high-temperature, Pb-free die-attach materials, J. Electron. Mater. 48 (1) (2019) 201–210.
[7] K.S. Siow, Are sintered silver joints ready for use as interconnect material in microelectronic packaging? J. Electron. Mater. 3 (4) (2014) 947–961.
[8] W. Zhang, J. Chen, Z. Deng, Z. Liu, Q. Huang, W. Guo, J. Huang, The pressureless sintering of micron silver paste for electrical connections, J. Alloys Compd. 795 (2019) 163–167.
[9] M. Myśliwiec, R. Kisiel, Thermal and mechanical properties of sintered Ag layers for power module assembly, Microelectron. Int. 32 (2015) 37–42.
[10] G. Chen, L. Yu, Y. Mei, X. Li, X. Chen, G.Q. Lu, Uniaxial ratcheting behavior of sintered nanosilver joint for electronic packaging, Mater. Sci. Eng. A 591 (2014) 121–129.
[11] T. Wang, G. Chen, Y. Wang, X. Chen, G.Q. Lu, Uniaxial ratcheting and fatigue behaviors of low-temperature sintered nano-scale silver paste at room and high temperatures, Mater. Sci. Eng. A 527 (2010) 6714–6722.
[12] S. Sakamoto, T. Sugahara, K. Suganuma, Microstructural stability of Ag sinter joining in thermal cycling, J. Mater. Sci. Mater. Electron. 24 (2013) 1332–1340.
[13] C. Chen, C. Choe, Z. Zhang, D. Kim, K. Suganuma, Low-stress design of bonding structure and its thermal shock performance (-50 to 250°C) in SiC/DBC power die-attached modules, J. Mater. Sci. Mater. Electron. 29 (2018) 14335–14346.
[14] W.S. Hong, M.S. Kim, C. Oh, Y. Joo, Y. Kim, K.K. Hong, Pressureless silver sintering of silicon-carbide power modules for electric vehicles, JOM 72 (2020) 889–897.
[15] P. Gadaud, V. Caccuri, D. Bertheau, J. Carr, X. Milhet, Ageing sintered silver: relationship between tensile behavior, mechanical properties and the nanoporous structure evolution, Mater. Sci. Eng. A 669 (2016) 379–386.
[16] X. Long, Z. Li, X. Lu, H. Guo, C. Chang, Q. Zhang, A. Zehri, W. Ke, Y. Yao, L. Ye, J. Liu, Mechanical behaviour of sintered silver nanoparticles reinforced by SiC microparticles, Mater. Sci. Eng. A 744 (2019) 406–414.
[17] X. Li, G. Chen, L. Wang, Y.H. Mei, X. Chen, G.Q. Lu, Creep properties of low-temperature sintered nano-silver lap shear joint, Mater. Sci. Eng. A 579 (2013) 108–113.
[18] S. Zabihzadeh, S. Van Petegem, M. Holler, A. Diaz, L.I. Duarte, H.V. Swygenhoven, Deformation behavior nanoporous polycrystalline silver. Part I: microstructure and mechanical properties, Acta Mater. 131 (2017) 467–474.
[19] F. Qin, Y. Hu, Y. Dai, T. An, P. Chen, Evaluation of thermal conductivity for sintered silver considering aging effect with microstructure based model, Microelectron. Reliab. 108 (2020) 113633.
[20] F. Qin, Y. Hu, Y. Dai, T. An, P. Chen, Y. Gong, H. Yu, Crack effect on the equivalent thermal conductivity of porously sintered silver, J. Electron. Mater. 49 (2020) 5994–6008.
[21] J. Ordonez-Miranda, M. Hermens, I. Nikitin, V.G. Kouznetsova, O.V.D. Sluis, M. A. Ras, J.S. Wagner, M. Sledzinska, J. Gomis-Bresco, C.M.S. Torres, B. Wunderle, S. Volz, Measurement and modeling of the effective thermal conductivity of sintered silver pastes, Int. J. Therm. Sci. 108 (2016) 185–194.
[22] C.J. Du, X. Li, Y.H. Mei, G.Q. Lu, An explanation of sintered silver bonding formation on bare copper substrate in air, Appl. Surf. Sci. 490 (2019) 403–410.
[23] S. Fu, Y.H. Mei, P. Ning, G.Q. Lu, Parametric study on pressureless sintering of nanosilver paste to bond large-area (≥100 mm2) power chips at low temperature for electronic packaging, J. Electron. Mater. 44 (10) (2015) 3973–3984.
[24] H. Zheng, D. Berry, K.D.T. Ngo, G.Q. Lu, Chip-bonding on copper by pressureless sintering of nanosilver paste under controlled atmosphere, IEEE Trans. Compon. Packag. Manuf. Technol. 4 (3) (2014) 377–384.
[25] X. Milhet, A. Nait-Ali, D. Tandiang, Y.J. Liu, D.V. Campen, V. Caccuri, M. Legros, Evolution of the nanoporous microstructure of sintered Ag at high temperature using in-situ X-ray nanotomography, Acta Mater. 156 (2018) 310–317.
[26] C. Chen, K. Suganuma, Microstructure and mechanical properties of sintered Ag particles with flake and spherical shape from nano to micro size, Mater. Des. 162 (2019) 311–321.
[27] V. Caccuri, X. Milhet, P. Gadaud, D. Bertheau, M. Gerland, Mechanical properties of sintered Ag as a new material for die bonding: influence of the density, J. Electron. Mater. 43 (12) (2014).
[28] I.L. Regalado, J.J. Williams, S. Joshi, E.M. Dede, Y. Liu, N. Chawla, X-ray microtomography of thermal cycling damage in sintered nano-silver solder joints, Adv. Eng. Mater. 21 (2019) 1801029.
[29] R. Khazaka, L. Mendizabal, D. Henry, Review of joint shear strength of nano-silver paste and its long-term high temperature reliability, J. Electron. Mater. 43 (7) (2014) 2459–2466.
[30] Y. Liu, H. Zhang, L. Wang, X. Fan, G. Zhang, F. Sun, Effect of sintering pressure on the porosity and the shear strength of the pressure-assisted silver sintering bonding, IEEE Trans. Device Mater. Reliab. 18 (2) (2018) 240–246.
[31] X. Li, G. Chen, X. Chen, G.Q. Lu, Mechanical property evaluation of nano-silver paste sintered joint using lap-shear test, Solder. Surf. Mt. Technol. 24 (2) (2012) 120–126.
[32] Y. Tan, X. Li, G. Chen, Q. Gao, G.Q. Lu, Effect of thermal aging on long-term reliability and failure modes of nano-silver sintered lap-shear joint, Int. J. Adhesion Adhes. 97 (1–7) (2020) 10288.
[33] C. Chen, S. Nagao, K. Suganuma, J. Jiu, T. Sugahara, H. Zhang, T. Iwashige, K. Sugiura, K. Tsuruta, Macroscale and microscale fracture toughness of microporous sintered Ag for applications in power electronic devices, Acta Mater. 129 (2017) 41–51.
[34] S. Wang, C. Kirchlechner, L. Keer, G. Dehm, Y. Yao, Interfacial fracture toughness of sintered hybrid silver interconnects, J. Mater. Sci. Mater. Electron. 55 (2020) 2891–2904.
[35] A.J. Russell, K.N. Street, Factors affecting the interlaminar fracture energy of graphite/epoxy laminates, in: Proceedings of the Fourth International Conference on Composite Materials, ICCM-IV Tokyo, Japan, 1982, pp. 279–286.
[36] B.D. Davidson, S.S. Teller, Recommendations for an ASTM standardized test for determining G_{IIC} of unidirectional laminated polymeric matrix composites, J. ASTM Int. 7 (2) (2010) 1–11.
[37] Y. Huang, W. Liu, Q. Jiang, Y. Wei, Y. Qiu, Interlaminar fracture toughness of carbon-fiber-reinforced epoxy composites toughened by poly (phenylene oxide) particles, ACS Appl. Polym. Mater. 2 (2020) 3114–3121.
[38] X. Han, Y. Chao, W. Zhang, Y. Chao, C. Wu, Study on the effect of post curing on the mode II fracture energy of structural adhesive using a parameter identification approach, Int. J. Adhesion Adhes. 95 (2019) 102398.
[39] J.A. Sousa, A.B. Pereira, A.P. Martins, A.B. de Morais, Mode II fatigue delamination of carbon/expoxy laminates using the end-notched flexure test, Compos. Struct. 134 (2015) 506–512.
[40] C. Chen, J. Yeom, C. Choe, G. Liu, Y. Gao, Z. Zhang, B. Zhang, D. Kim, K. Suganuma, Necking growth and mechanical properties of sintered Ag particles with different shapes under air and N_2 atmosphere, J. Mater. Sci. 54 (2019) 13344–13357.
[41] Y. Akada, H. Tatsumi, T. Yamaguchi, A. Hirose, T. Morita, E. Ide, Interfacial bonding mechanism using silver metallo-organic nanoparticles to bulk metals and observation of sintering behavior, Mater. Trans. 49 (7) (2008) 1537–1545.
[42] L.F.M. da Silva, F.A.C.R.G. de Magalhães, F.J.P. Chaves, M.F.S.F. de Moura, Mode II fracture toughness of a brittle and ductile adhesive as a function of the adhesive thickness, J. Adhes. 86 (2010) 891–905.
[43] J.C.P. Tueiredo, R.D.S.G. Campilho, E.A.S. Marques, J.J.M. Machado, L.F.M. da Silva, Adhesive thickness influence on the shear fracture toughness measurements of adhesive joints, Int. J. Adhesion Adhes. 83 (2018) 15–23.
[44] M.F.S.F. de Moura, A.B. de Morais, Equivalent crack based analyses of ENF and ELS tests, Eng. Fract. Mech. 75 (2008) 2584–2596.
[45] J.C.S. Azevedo, R.D.S.G. Campilho, J.F.G. da Silva, T.M.S. Faneco, R.M. Lopes, Cohesive law estimation of adhesive joints in mode II condition, Theor. Appl. Fract. Mech. 80 (2015) 143–154.
[46] J. Wang, P. Qiao, Novel beam analysis of end notched flexure specimen for mode II fracture, Eng. Fract. Mech. 71 (2004) 219–231.
[47] J. Li, C.M. Johnson, C. Buttay, W. Sabbah, S. Azzopardi, Bonding strength of multiple SiC die attachment prepared by sintering of Ag nanoparticles, J. Mater. Process. Technol. 215 (2015) 299–308.
[48] S.T. Chua, K.S. Siow, Microstructural studies and bonding strength of pressureless sintered nano-silver joints on silver, direct bonding copper (DBC) and copper substrates aged at 300°C, J. Alloys Compd. 687 (2016) 486–498.
[49] C. Chen, K. Suganuma, T. Iwashige, K. Sugiura, K. Tsuruta, High-temperature reliability of sintered microporous Ag on electroplated Ag, Au, and sputtered Ag metallization substrates, J. Mater. Sci. Mater. Electron. 29 (2018) 1785–1797.
[50] Z.Z. Fang, H. Wang, V. Kumar, Coarsening, densification, and grain growth during sintering of nano-sized powder-A perspective, Int. J. Refract. Met. H 62 (2017) 110–117.
[51] S.J. Park, J.M. Martin, J.F. Guo, J.L. Johnson, R.M. German, Grain growth behavior of tungsten heavy alloys based on the master sintering curve concept, Metall. Mater. Trans. A Phys. Metall. Sci. 37 (2006) 3337–3346.
[52] S.Y. Gómez, D. Hotza, Predicting powder densification during sintering, J. Eur. Ceram. Soc. 38 (2018) 1736–1741.
[53] R. German, Sintering: from Empirical Observations to Scientific Principles, Butterworth-Heinemann, 2014.
[54] B.N. Kim, T.S. Suzuki, K. Morita, H. Yoshida, Y. Sakka, H. Matsubara, Densification kinetics during isothermal sintering of 8YSZ, J. Eur. Ceram. Soc. 36 (2016) 1269–1275.
[55] S. Joo, D.F. Baldwin, Adhesion mechanisms of nanoparticle silver to substrate materials: identification, Nanotechnology 21 (2010), 055204.
[56] L.K. Singh, A. Bhadauria, S. Jana, T. Laha, Effect of sintering temperature and heating rate on crystallite size, densification behaviour and mechanical properties of Al-MWCNT nanocomposite consolidated via spark plasma sintering, Acta Metall. Sin. 31 (2018) 1019–1030.
[57] A.A. Griffith, The phenomena of rupture and flow in solids, Phil. Trans. ser. A 221 (1920) 13–198.

[58] M. Gu, H. Xu, J. Zhang, Z. Wei, A. Xu, Influence of hot pressing sintering temperature and time on microstructure and mechanical properties of TiB_2/TiN tool material, Mater. Sci. Eng. A 545 (2012) 1–5.
[59] R. Eatemadi, Z. Balak, Investigating the effect of SPS parameters on densification and fracture toughness of ZrB_2-SiC nanocomposite, Ceram. Int. 45 (2019) 4763–4770.
[60] N. Chawla, X. Deng, Microstructure and mechanical behavior of porous sintered steels, Mater. Sci. Eng. A 360 (2005) 98–112.
[61] L.J. Gibson, M.F. Ashby, Cellular Solids: Structure and Properties, Cambridge University Press, 1999.
[62] Q.D. Yang, M.D. Thouless, S.M. Ward, Elastic-plastic mode-II fracture of adhesive joints, Int. J. Solid Struct. 38 (2001) 3251–3262.